International Journal of Heat and Mass Transfer 216 (2023) 124556

Contents lists available at ScienceDirect

International Journal of Heat and Mass Transfer

journal homepage: www.elsevier.com/locate/ijhmt

Experimental study on subcooled pool boiling of FC-72 on a flat plate in normal and microgravity

Peng Liu [a,c,1], Ke Wu [a,c,1], Wang-Fang Du [a,c,*], Hui-Xiong Li [b], Jian-Fu Zhao [a,c]

[a] CAS Key Laboratory of Microgravity, Institute of Mechanics, Chinese Academy of Sciences. Beijing 100190, China
[b] State Key Laboratory of Multiphase Flow in Power Engineering, Xi'an Jiaotong University, Xi'an 710049, China
[c] School of Engineering Science, University of Chinese Academy of Sciences, Beijing 100049, China

ARTICLE INFO

Keywords:
Pool boiling
Microgravity
Heat transfer
SJ-10 satellite
Single-phase convection
Critical heat flux

ABSTRACT

A series of experimental studies on the heat transfer characteristics of pool boiling were conducted aboard the Chinese satellite SJ-10 in April 2016. Ground comparative experiments under the same conditions were carried out using the same apparatus. FC-72 was used as the working fluid containing non-condensable gas. The total quasi-stable-state acceleration aboard satellite SJ-10 during its in-orbit flight is approximately 2×10^{-6} g_0. The integrated microheater fabricated by the microelectromechanical system (MEMS) technique was used to investigate the boiling characteristics. The boiling surface of the integrated microheater is on top of a flat plate quartz glass wafer substrate 2 mm thick, heated by a serpentine Pt thin film (main heater) below the substrate. The effective area of the boiling surface in direct contact with FC-72 is 5.5 mm in diameter. Ten temperature sensors are located around the boiling surface center and uniformly distributed in the circumferential direction. The experimental results show that single-phase convection could still be maintained under lower Rayleigh number conditions, showing consistency with the predictions based on the available correlations. The generated bubble volume determines the boiling state. At high liquid subcooling, the bubbles formed after the liquid vaporizes are relatively small, and steam condensation at the bubble cap promotes the phase change efficiency, which maintains nucleate boiling in microgravity. When subcooling is low, bubbles are larger and cover most of the heating surface, nucleate boiling is difficult to maintain, and the boiling becomes transition boiling. High liquid subcooling improves the heat transfer efficiency, thereby contributing to maintaining the progress of nucleate boiling in microgravity. However, boiling is less affected by liquid subcooling on the ground than in microgravity. A comparison of pool boiling curves between microgravity and normal gravity experiments indicates that nucleate boiling curves under the same subcooling partially overlap, while the heat flux corresponding to the initiation of the nucleate state is lower than that on the ground. In microgravity, lower liquid subcooling and higher heating power will result in larger bubble volumes and easier complete coverage of the heating surface, resulting in an easier transition from nucleate boiling to film boiling.

1. Introduction

Boiling is one of the most effective methods of heat transfer and is widely employed in component cooling and various energy conversion systems. There also exist many potential applications of boiling in the thermal control and management systems of in-orbit satellites and other large spacecraft, e.g., space stations and deep-space explorers, to achieve better heat transfer performance in microgravity. Boiling is a very complex process due to the interrelation of numerous factors, such as the roughness of the heating surface, liquid properties, liquid subcooling, pressure, and gravity. The usefulness of classical correlations of boiling heat transfer, such as the Rohsenow correlation for nucleate pool boiling, quickly diminishes as parameters of interest start to fall outside the range of physical parameters for which the correlations were developed. Progress in the international space industry demands a better understanding of the effect of gravity on boiling heat transfer. Microgravity research can provide a basic scene in which the effects of gravity on boiling are severely suppressed and can then be conducive to revealing the mechanisms underlying the phenomena.

Research on boiling in microgravity has a history of more than 60 years since the 1960s. The characteristics of nucleate pool boiling in

* Corresponding author at: CAS Key Laboratory of Microgravity, Institute of Mechanics, Chinese Academy of Sciences. Beijing 100190, China.
E-mail address: duwangfang@imech.ac.cn (W.-F. Du).
[1] These authors have made the same contributions to this paper.

https://doi.org/10.1016/j.ijheatmasstransfer.2023.124556
Received 15 February 2023; Received in revised form 3 July 2023; Accepted 27 July 2023
Available online 6 August 2023

Nomenclature

c_g	non-condensable gas concentration (ppm)
Δx	thickness of the substrate of the integrated micro heater (m)
g_0	terrestrial gravity (m/s^2)
H	Henry's constant (mole/(mole·Pa))
h	heat transfer coefficient (W/(m^2·K))
L_h	characteristic length (m)
Nu	Nusselt number (-)
Ra	Rayleigh number (-)
Gr	Grashof number (-)
Pr	Prandlt number (-)
p	liquid pressure (kPa)
q	heat flux (W/cm^2)
T	temperature (°C)
T_i	temperature at the i th local temperature sensor (°C)
CHF	critical heat flux (W/cm^2)

Greek

α	thermal diffusivity (m^2/s)
β	volume expansion coefficient (K^{-1})
λ	thermal conductivity (W/(m·K))
ρ	density (kg/m^3)
τ	time (s)
ν	kinematic viscosity (m^2/s)
c_p	specific heat capacity (J/(kg·K))
μ	dynamic viscosity (Pa·s)
σ	surface tension coefficient (N/m)
h_{fg}	latent heat of vaporization (kJ/kg)

Subscripts

bulk	bulk liquid
back, b	back-side of the substrate of the integrated micro heater
top, t	top-side of the substrate of the integrated micro heater
sat	saturation
sub	subcooling
wall	inner wall of the boiling chamber
v	vapor
l	liquid

microgravity have been investigated by various research groups. Many comprehensive reviews on the progress in this field, for example, those by Straub [1], Di Marco and Grassi [2], Kim [3], Ohta and Baba [4], Colin et al. [5], Zhao [6] and Hong [7], among many others, are now available. Thus, only recent studies closely relevant to the present study are summarized here.

Among all the kinds of working fluids used in previous experimental studies, FC-72 is commonly utilized in microgravity experiments because it has a lower boiling point and is chemically stable. Experiments on pool boiling of FC-72 or n-perfluorohexane at 1 bar on flat heaters were conducted by Kim et al. [8], Henry and Kim [9], Henry et al. [10], Raj and Kim [11], and Raj et al. [12–14] in KC-135 parabolic flights. Boiling bubble behavior as well as contact line movement was recorded from the side and bottom of the heater. During the parabolic flights, the experiments went through a high-g (1.8 g_0) process and a 25 s low-g (10^{-2} g_0) process. The effects of the gravity level, subcooling, heater size and dissolved gas concentration on pool boiling heat transfer were investigated in these experiments. Moreover, Raj et al. [15] conducted pool boiling experiments of n-perfluorohexane in the Microheater Array Boiling Experiment (MABE) facility aboard the International Space Station (ISS). The heating element was a 7×7 mm^2 microheater array. Apart from all the factors that affect boiling heat transfer described in previous works, the effect of pressure was also investigated during the in-orbit experiment. From these works, a gravity scaling parameter was developed to predict the microgravity boiling heat transfer process from boiling data obtained in earth gravity experiments.

To avoid the effect of the heater edge, Kawanami et al. [16] used a larger transparent heater array, which was 76 mm in diameter and 2 mm in thickness, with 88 pairs of temperature sensors and a mini-heater to observe the local heat transfer and vapor bubble dynamics in microgravity pool boiling aboard the ESA 49th parabolic flight. The bubble behavior was found to be strongly affected by the fluctuation of gravity in low g and affected the heat transfer performance differently in various liquid subcooling conditions. At high subcooling, heat transfer was enhanced in the positive low-g period because of the enhancement of microlayer evaporation and decreased in the negative low-g period because of bubble detachment. However, under low subcooling conditions, the trend was reversed: in the positive low-g period, bubbles became larger, and a dry patch formed underneath the bubbles, leading to deterioration of heat transfer, and in the negative low-g period, the heat flux increased because of enhanced bubble detachment.

Dhir et al. [17] and Warrier et al. [18] reported results of the Nucleate Pool Boiling eXperiments (NPBX), also housed in the Boiling eXperiment Facility (BXF) on the ISS. The microgravity varied from 1.7 $\times$ 10^{-7} g_0 to 6 $\times$ 10^{-7} g_0 during the in-orbit flight. The heating element was a 1 mm thick and 89.5 mm diameter aluminum wafer with five cavities located on the surface. The working fluid was n-perfluorohexane, with the dissolved gas concentration varied from 46 ppm to 737 ppm. In the nucleate boiling regime, a large bubble formed from the coalescence of multiple bubbles, moved to the middle of the heater surface and acted as a vapor sink absorbing smaller bubbles generated on the surface. The normalized heat transfer coefficients for nucleate pool boiling were found to be weakly dependent on the gravity level. The heat transfer rate in microgravity was compared to the literature results and was found to depend on the heater size and fluid confinement. Although the NPBX and MABE experiments were both carried out in the same device on the ISS, the heating surfaces used by the two were different, and the obtained heat transfer boiling curve data differed between the two; thus, they cannot be directly compared.

Zhao et al. [19] investigated pool boiling of FC-72 in microgravity by using a flat 15 $\times$ 15 mm^2 Al_2O_3 ceramic substrate with a multi-metal alloy heater. The experimental facility was aboard the Chinese recoverable satellite SJ-8, which could supply a microgravity condition of a gravity level between 10^{-3} g_0 and 10^{-4} g_0 during in-orbit flight. At high subcooling, boiling bubbles had smooth surfaces and small sizes, so nucleate boiling and local dry areas coexisted on the surface. At low subcooling, bubble nucleation was intensified by the surface oscillation of the coalesced bubbles. The critical heat flux (CHF) values obtained in microgravity were only approximately one-third of those in terrestrial conditions under similar pressure and subcooling. Moreover, Xue et al. [20] studied the nucleate pool boiling of subcooled FC-72 on a smooth square silicon chip with dimensions of 10 $\times$ 10 $\times$ 0.5 mm^3 in short-term microgravity utilizing the Beijing drop tower and in normal gravity. An experimental study of pool boiling heat transfer was conducted for micro-pin-finned surfaces with different pitches (45, 60, and 75 μm) and configurations by Zhang et al. [21]

Di Marco and Grass [22–23] conducted pool boiling experiments of FC-72 on a heating element consisting of a square 20 $\times$ 20 mm^2 layer of 40 nm thick gold sputtered over a ZnS substrate in the presence of an electric field in terrestrial and reduced gravity. A microgravity environment of 10^{-4} g_0 or lower was obtained during the in-orbit flight of the

Foton-M2 unmanned space mission. The analysis of the boiling patterns showed that the void fraction in microgravity was increased compared to that in terrestrial conditions. Although nucleate boiling could still occur in micro-g, the heat transfer performance was partially degraded. With the application of an external electrostatic field, boiling heat transfer was significantly improved under both normal and microgravity conditions.

Schweizer et al. [24] investigated the wall temperature and heat flux distributions on a 25 μm stainless foil during nucleate boiling in the presence of an electric field and in variable gravity. The microgravity results were obtained during the 50th ESA parabolic flight. The temperature distribution was measured via infrared (IR) thermography, and the local heat flux to the liquid was computed by applying an unsteady energy balance. The boiling bubbles did not detach from the heating surface due to the absence of buoyancy in microgravity, and a rapidly heating adsorbed film region surrounded by a cool evaporating region formed in parabolic flight experiments.

The behavior of a single vapor bubble of FC-72 in microgravity was investigated by Fisher et al. [25] The microgravity experiments were carried out on the 53rd ESA Parabolic Flight Campaign aboard the Airbus A300 Zero-G, which could provide 22 s of a microgravity environment of -5 $\times$ 10^{-2} g_0 to 5 $\times$ 10^{-2} g_0. The flat heater with an artificial nucleation site consisted of a CaF_2 substrate coated with a heating layer of pure chromium and a chromium-based emissivity layer, which realized IR thermography measurement of the local temperature under a single growing vapor bubble. A local temperature drop and a high heat flux could be observed in the three-phase contact line region by using the heater with a higher thermal capacity, in which the behavior was similar to that with a thin heating element. The influence of liquid subcooling of single vapor bubble was discussed by Narayan et al. [26,27]. The bubble dynamics characteristics of isolated single bubble in subcooled de-ionized water were investigated, and the condensation and thermal capillary convection characteristics of bubbles were revealed. Moreover, microlayer dynamics during the growth process of a single bubble under subcooled nucleate flow boiling was reported by Sinha et al. [28]. These works highlighted the importance of subcooled liquid conditions during the complex phenomena of nucleate pool boiling heat transfer.

Recently, a multiscale boiling investigation which is called RUBI was conducted on the ISS by Sielaff et al. [29] and Nejati [30]. A detailed investigation of the growth of bubbles, the influence of shear flow, and the influence of an electric field within the same test facility using FC-72 as the working fluid was performed. Further work is being done on sharing and optimizing evaluation algorithms and procedures, focusing on specific aspects of the bubble behavior in various boiling situations [31,32].

Similar to the expounded previous projects, to study the bubble dynamics in isolated single bubble pool boiling and the local heat transfer inside the heating element during the boiling process, we developed the facility SOBER-SJ10 (Single bubble pOol Boiling ExpeRiment aboard SJ-10), utilizing an integrated microheater as the heating and measuring element. The former ground experiment results and measurement methodology were reported by Wu et al. [33]. In-orbit pool boiling experiments were successfully conducted in April 2016. The data from the single bubble and normal pool boiling experiments were carefully analyzed afterward. In this paper, only the normal pool boiling experiment results are presented, including the single-phase heat transfer performance, nucleate pool boiling process in microgravity, nucleate pool boiling curve in normal and microgravity and film boiling results in microgravity. The present results are mainly compared to classical heat transfer coefficients and previous studies that also used FC-72 as a working fluid to avoid discussing the effects of liquid properties on boiling heat transfer in the present paper. The comparison of pool boiling curves of FC-72 shows the effects of the heater size, degree of subcooling and non-condensable gas concentration on pool boiling heat transfer.

Note that although the existing microgravity boiling experimental results have indicated that microgravity boiling can stably exist with properties quite different from the theory based on terrestrial research, due to the complicated factors of boiling, the existing microgravity experiments, whether space experiments or ground-based short-term microgravity experiments, can only be limited to a binary comparison of boiling in the presence and absence of gravity [34]. Gravity in these studies cannot be used as an independent variable, which makes revealing the mechanism of gravity in boiling difficult.

2. Experimental facility

SOBER-SJ10 is one of the 27 selected experiments in the mission SJ-10 [35]. The SOBER-SJ10 device, with an outer envelope size of 400 mm $\times$ 296 mm $\times$ 280 mm and a total weight of 24.8 kg, is mainly composed of an air-proof capsule, a boiling cha36mber, an electric control box (ECB) and two charge-coupled device (CCD) components (Fig. 1). The latter three components are installed inside the air-proof capsule, which is made of aluminum alloy. The pressure inside the air-proof capsule is nominally 100 kPa, while the external pressure of the device is approximately 48 kPa aboard the SJ-10 satellite in orbit [36].

2.1. Boiling chamber and its accessory components

A schematic of the boiling chamber is shown in Fig. 2. Its main accessory components include a liquid chamber, a cover plate with two end caps, a bellows as the pressure regulator, eight film preheaters, an integrated microheater, a pre-data acquisition board (pre-DAB) along with its support, three light-emitting diode (LED) lighting components, two observation components, and an electric connector. Detailed description is available in Wu et al. [33].

The total height of the liquid chamber is 234 mm, while its cross-section is designed as a regular octagon with an inscribed circle diameter of 150 mm to facilitate the installation of the accessory components. Degassed FC-72 with an effective volume of approximately 2.8 L is filled inside the liquid chamber, acting as the working fluid. Eight film preheaters with a total heating power of 60 W are fixed on the outer walls of the chamber, which are used to adjust the bulk liquid temperature from the ambient temperature to a nearly saturated value at the corresponding pressure. Two Pt1000 resistance temperature detector (RTD) temperature sensors fixed on the inner wall are used to adjust the liquid temperature in the boiling chamber.

The integrated microheater, which will be described in detail in the following section, is fixed at the center of the pre-DAB, which is installed at the bottom of the liquid chamber with an inclination angle of 15° Two Keller® PAA-4LD digital absolute pressure sensors are fixed on the two sides of the integrated microheater, which are used to simultaneously measure the pressure inside the boiling chamber and the temperature of the bulk liquid near the integrated microheater. For the bulk liquid temperature measurements, the uncertainties are ±0.2 °C in the range from 20 °C to 80 °C according to the pre-calibration results.

Three LED lighting components and two observation components are alternately set in front of the heater. A beryllium bronze bellows, which is welded on the cover plate, acts as a pressure regulator to maintain the pressure inside the liquid chamber approximately constant during the preheating and boiling processes with the help of a constant background pressure environment inside the air-proof capsule.

2.2. Integrated microheater

The integrated microheater is fabricated by the MEMS technique. The substrate of the integrated microheater is a 10 mm $\times$ 10 mm $\times$ 2 mm quartz glass wafer. The thickness of 2 mm was determined based on a prior numerical study by Zhang et al. [37] and Li et al. [38]. Fig. 3 shows the electronic circuit configurations, which were fabricated by using the

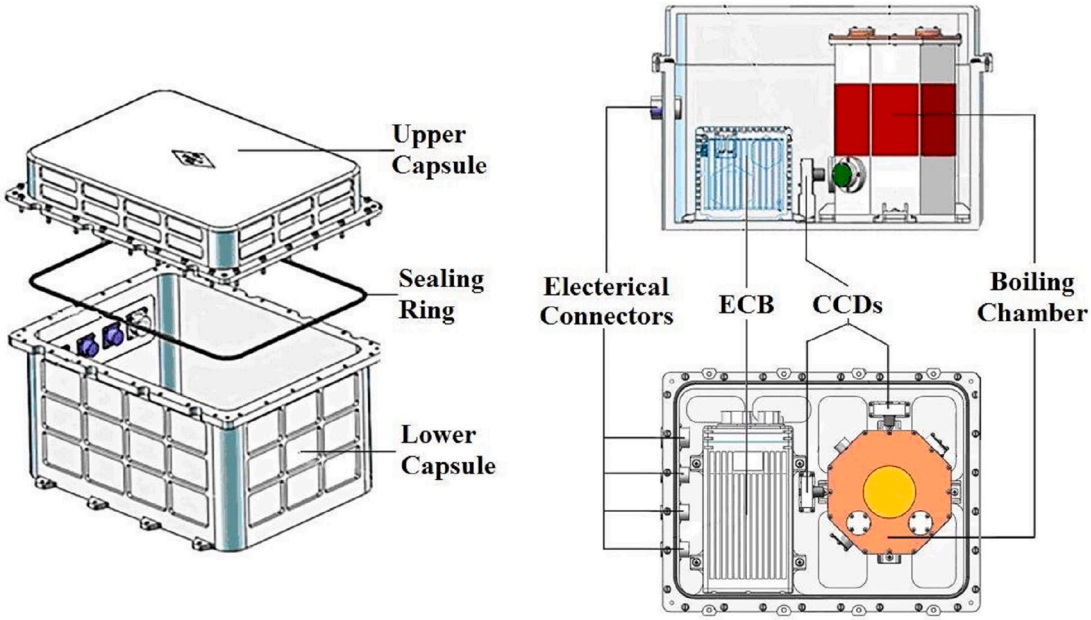

Fig. 1. Schematic of the experimental facility.

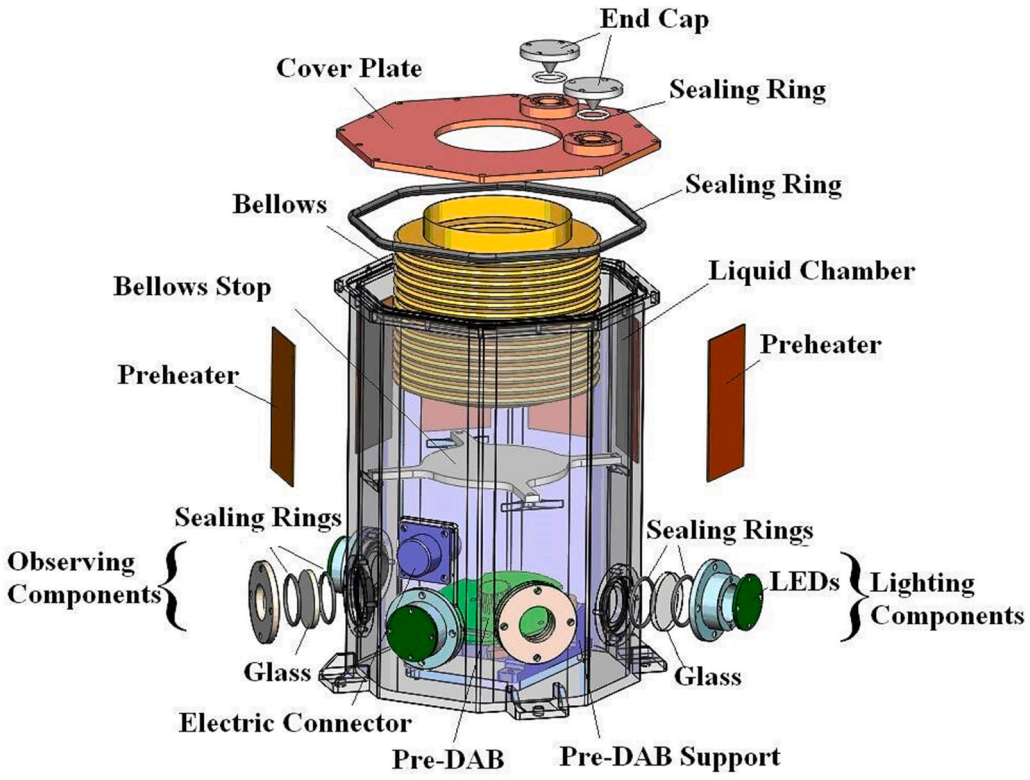

Fig. 2. Exploded view of the boiling chamber.

standard photolithography technique for patterning of the sensor design and magnetron sputtering for film deposition on the top and back sides of the substrate. The top side here refers to the side directly contacting the liquid.

At the center of the top side, there is a pulse-heating bubble trigger (BT) to excite a bubble nucleus by using the method of local overheating (Fig. 3c). Around the BT, there are ten RTDs for measurement of the local temperature on the heater surface, as shown in Fig. 3b, which are uniformly distributed in the circumferential direction. The distances of these local temperature sensors from the center of the BT are listed in Table 1. For the sake of safety, the BT is composed of two parallel platinum films with a size of 100 μm × 20 μm and a spacing of 20 μm. Each local temperature sensor is composed of a serpentine strip of a platinum film covering an area of 55 μm × 50 μm.

On the back side of the substrate, as shown in Fig. 3d, a serpentine strip of a platinum film of approximately 5000 Å in thickness acts simultaneously as the main heater to provide the input power for maintaining the boiling process and the temperature sensor to measure

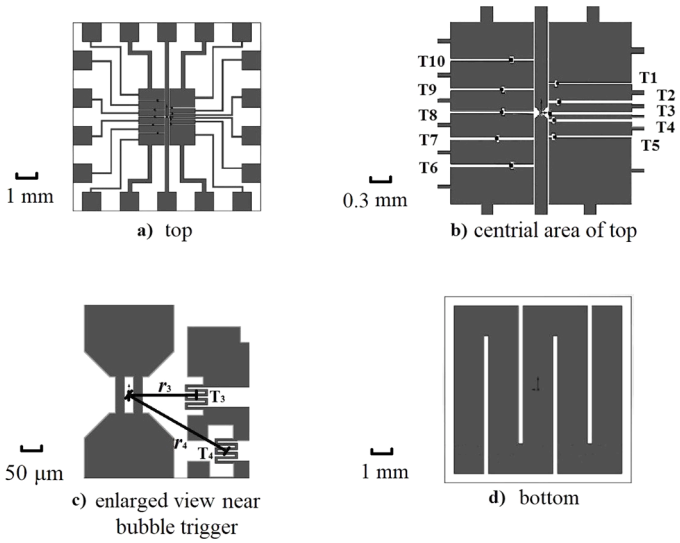

Fig. 3. Circuit configurations on the substrate of the integrated microheater: a) top-side view, b) enlarged view of the center on the top side, c) enlarged view near the bubble trigger, d) main heater on the back side.

the average temperature on the back side of the substrate, which will be used in the evaluation of the heat flux to the working fluid.

A kind of plastic package, chip on board (COB) encapsulation, is used to encapsulate the integrated microheater as an independent electronic component (Fig. 4). Two printed circuit boards (PCBs) of 1.6 mm thickness are used to provide electric connections and mechanical support for the integrated microheater. The substrate, as well as all gold wires, is packaged on the PCBs by using the packaging adhesive DOVER DE108. An uncovered test area with a diameter of approximately 5.5 mm can directly contact the liquid, which is referred to as the heater surface in the following. It is slightly lower than the chip surface.

Fig. 5 shows the circuit principle diagram relevant to the integrated microheater. The 10 local temperature sensors are divided into 2 groups. Each group has 5 sensors connected in series to a set of parallel precision resistors (RM11 or RM12). Each set has two precision resistors with a nominal resistance of 1000.0 Ω and a precision of 0.01%, acting as a reference resistance to measure the current across it and the local temperature sensors in the same circuit loop. The voltages across the local temperature sensors are then used to calculate the resistances of the sensors, which provide measurements of the temperature at the locations of the sensors based on the calibrated relationship between the temperature and the resistance of each sensor.

The BT is connected to the pulse power supply (P-1) through a protective resistor (R01), while the main heater is connected to the

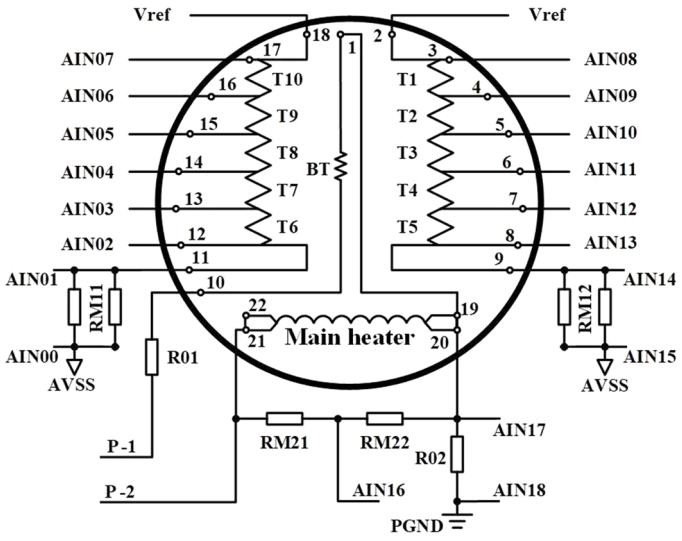

Fig. 5. Circuit principle diagram relevant to the integrated microheater.

Table 1
The distances r_i of local temperature sensors from the center of the bubble trigger.

No.	T1	T2	T3	T4	T5	T6	T7	T8	T9	T10
r_i (mm)	0.55	0.35	0.15	0.25	0.45	1.00	0.85	0.65	0.75	1.00

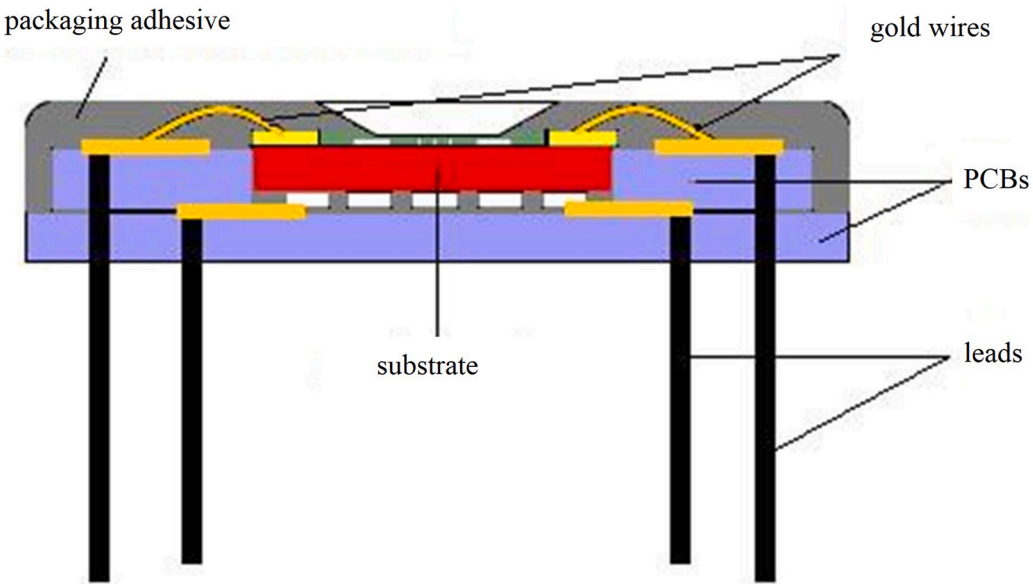

Fig. 4. Schematic of the integrated micro heater with a COB package (not to scale).

adjustable power supply (P-2). They are all connected to a precision resistor (R02) with a nominal resistance of 0.43 Ω and a precision of 0.1%, which acts as a reference resistance to measure the current across it. Two series precision resistors (RM21 and RM22) with a much larger resistance of 4.7 kΩ than the main heater (4 Ω) are connected in parallel to the main heater. The voltages across resistor RM22 are used to calculate the resistance of the main heater, which can provide measurements of the average temperature on the back side of the substrate of the integrated microheater based on the calibrated relationship between the temperature and the resistance of the main heater.

2.3. Data acquisition and video records

Analog signals, including the voltages relevant to the integrated microheater and the outputs from the sensors of the experiment, are sampled, encoded, packaged, and transmitted to the payload manager in the sealed module of satellite SJ-10. Since the facility SOBER-SJ10 cannot be recovered after space flight, all the data and the recorded video images are transmitted back to the ground through the remote transmission system when the satellite SJ-10 flies over mainland China.

A high sampling frequency of 500 Hz is used during the boiling phase for the signals relevant to the integrated microheater, namely, the voltages across the 10 local temperature sensors, main heater, and 3 reference resistances for the corresponding current measurements to obtain an adequate time resolution.

Two Watec® WAT-660D CCDs are installed in two orthogonal directions to obtain videos of the shape and motion of the growing bubble, which can be used to reconstruct the true shape of the growing bubble. Furthermore, these images can act as a redundancy backup for each other to improve reliability. The video is recorded at a sampling rate of 25 fps (frames per second). The analog video signals of the two CCD cameras are first converted into BT656 digital video signals and then encoded by using H.264 video compression format with a resolution of 720 (H) × 480 (V) pixels. The two compressed digital video signals, as well as the high-frequency sampling data mentioned above, are packaged by the FPGA unit and then transmitted to the payload manager through an LVDS interface.

3. Experimental procedure and data reduction

3.1. Experimental procedure

The planned space experiment lasts for approximately 15 h and is divided into 5 stages according to the bulk liquid temperature. Except for the first stage, which is carried out at ambient temperature, the other four stages begin with a preheating phase to adjust the bulk liquid temperature to 4 different design levels, namely, 35, 40, 45, and 50 °C. The adjusted range of the bulk liquid temperature is verified to be no more than ±1.0 °C on the ground. A slightly wider range or overshooting of the bulk liquid temperature is evident in space experiments compared with ground experiments, caused by the deterioration of natural convection in microgravity.

There are two boiling modes designed in the experiments. One is the so-called single bubble boiling mode, in which a bubble nucleus will be excited by the activated pulse BT and then grow under the heating of the main heater on the back side of the substrate of the integrated microheater. The input of the heating voltage is kept constant throughout each phase with a period of 180 s and is increased step-by-step in the successive phases. The other is the normal pool boiling mode, in which the BT is not activated, while the input of the heating voltage of the main heater is adjusted, increasing step by step. The period of each step successively decreases from the maximum value of 150 s at the lowest heating power to the minimum value of 60 s at the highest heating power. As shown in Fig. 6, there are 5 boiling phases (B.1 ~ B.5) in each stage, among which the first 4 boiling phases are designed as the single bubble boiling mode, while the last phase is the normal pool boiling

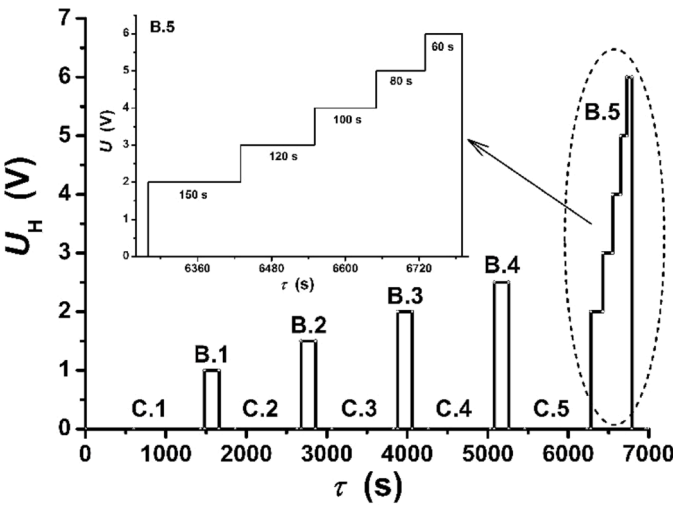

Fig. 6. Designed heating voltages on the main heater in a typical stage.

mode. For brevity, abbreviations of the boiling phases, such as GE7/2.5 and SE1/3.2, are used in the following sections. Here, GE7/2.5 refers to the fifth boiling phase of the second stage in the seventh ground experiment, while SE1/3.2 refers to the second boiling phase of the third stage in the first space experiment. Before each boiling phase, there is a calm phase (C.1 ~ C.5) to achieve a uniform temperature field in the vicinity of the integrated microheater. The first calm phase has the longest duration of approximately 30 min to achieve a uniform temperature after liquid preheating, while each of the other four calm phases lasts for 15 min for recovery of the temperature field near the heater after the previous phase of single bubble boiling.

In addition to completing the whole experimental process stage by stage, it can also be started from the beginning of any stage by manually adjusting the timing code. Fig. 7 shows the variation in the bulk liquid temperature, pressure inside the liquid chamber and corresponding saturated temperature in space experiments. In total, 4 space experiments with the same parameters were conducted during space flight after the successful launch of the recoverable satellite SJ-10 on April 6, 2016. The first space experiment (SE1) performed on April 10 is the planned experiment with the whole process of 15 h. The others are extended space experiments with only one stage of 3.5 h, which were

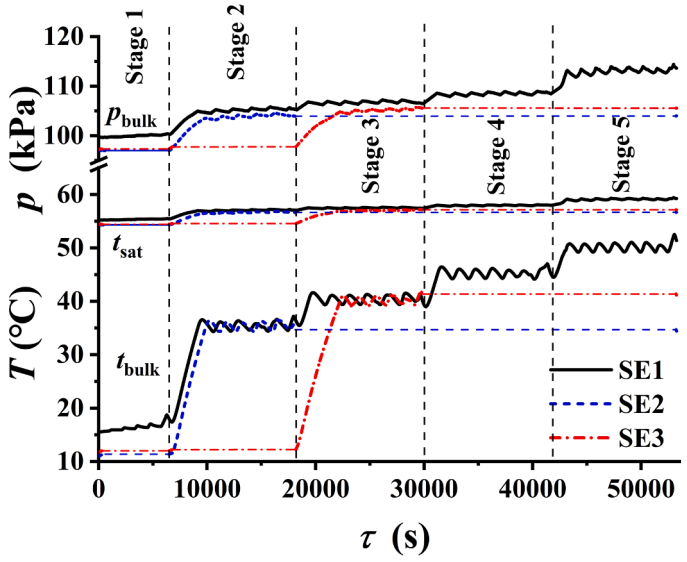

Fig. 7. Variations in the bulk liquid temperature, pressure inside the liquid chamber and corresponding saturated temperature in space experiments.

performed on April 19 (SE2), 23 (SE3), and 25 (SE4). Although the telemetry parameters indicate that it started off successfully, the scientific data of the last experiment (SE4) were not transmitted back to the ground because the electricity of the satellite battery ran out. Thus, scientific data are available only for the first three space experiments. In addition, 7 ground experiments, referred to as GE1 to GE7, were performed on the ground before the space flight.

3.2. Syn-Calibration of temperature sensors of the integrated microheater

As mentioned above, both the main heater and local temperature sensors of the integrated microheater are made of thin platinum films, which may exhibit obvious zero shifts. To avoid the effects of zero shifts on the calculated values of the measured temperatures, a syn-calibration procedure for the main heater and local temperature sensors has been proposed for the calibrations on the ground [33], in which the synchronous data sampled in the corresponding experiments with a negligible electric heating effect or even without any effect of heat input from both the main heater of the integrated microheater inside the working fluid and the preheaters outside the boiling chamber are used.

Fig. 8 shows, for example, the syn-calibrations for local temperature sensor T6 in the ground experiments before the space flight. The average bulk liquid temperature based on the temperature outputs from two Keller® PAA-4LD digital absolute pressure sensors is used as the reference temperature. Fig. 8 shows that there exists an obvious zero shift with a systematic trend. The uncertainties of local temperature sensors, however, are confirmed to be less than ±1.0 °C by using the syn-calibration procedure. Furthermore, caused by the uncertainty in the pressure measurement, the uncertainty of the saturated temperature of FC-72 is ±0.5 °C. Thus, the uncertainty of the wall superheat is no more than ±1.5 °C.

However, in space experiments, an unexpected change in the temperature-resistance relationship of the local sensors and the main heater occurred. Fig. 9 shows, for example, the comparison of the resistances of the same local temperature sensor T6 obtained from SE1 and GE7. The measurements of the bulk liquid temperature in both experiments are also shown in the same figure. Generally, the resistances of the local temperature sensors, corresponding to the temperature of the heater surface, are higher in space than their counterparts on the ground, which is caused by the deterioration of heat transfer in microgravity. Compared to the resistances before the corresponding boiling phase, obvious drops in the resistances are observed when the heating power is switched off, which cannot be observed in the ground experiments. Furthermore, the resistances in the following stages are obviously lower in space experiments than those in the corresponding stages

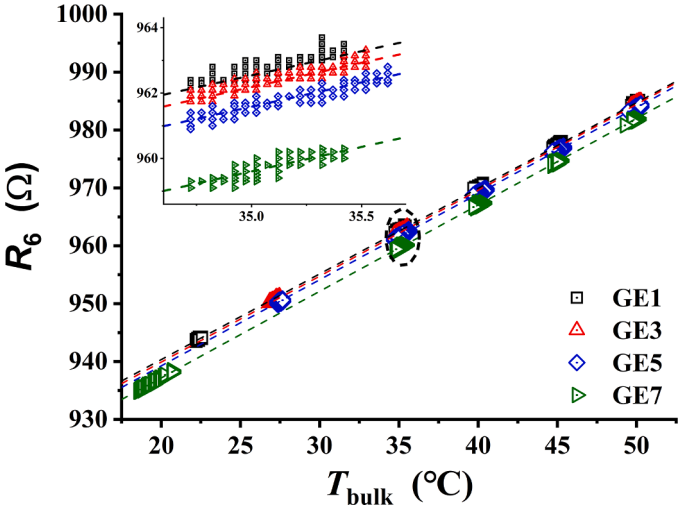

Fig. 8. Typical syn-calibrations of local temperature sensor T6 on the ground.

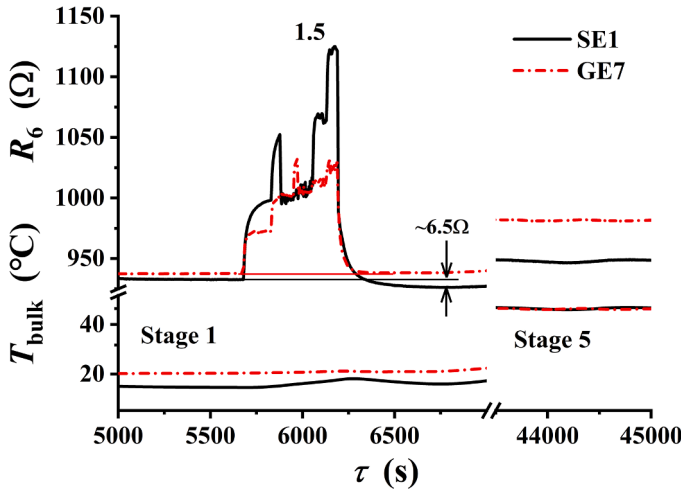

Fig. 9. Typical changes in the resistance of local temperature sensor T6 in SE1 and GE7.

with the same bulk liquid temperature in both ground experiments and previous space experiments. The combined action of the overheating in the normal pool boiling phase in each stage and the subsequent strong cooling process may cause some effect of annealing of the thin Pt film of the sensors, resulting in increasing electrical conductivity of the thin film sensors and decreasing resistance. The syn-calibration procedure mentioned above is then not applicable to data reduction in space experiments, even though it is successfully applied to data reduction in ground experiments.

Based on detailed data analysis, a modified syn-calibration procedure is proposed to achieve an accurate temperature-resistance relationship of local temperature sensors, which is used in the following data reduction process.

First, the temperature coefficients of the resistances, or the slopes of the linear fitting curves of the resistances versus the corresponding temperature, are determined by averaging the following two kinds of data for each sensor. As shown in Fig. 10, the first kind is the quasi-steady-state data during the preheating phases, including the first preheating phase S1 in SE1 and the preheating phases S2 and S3 in SE2 and SE3, respectively. The second kind is the steady-state data without the influence of the combined action of overheating and the subsequent strong cooling process. The available steady-state data, S4′/S4 in SE2 and S5′/S5 in SE3, are found only in the extended space experiments SE2 and SE3, in which there is no boiling phase before the preheating phase

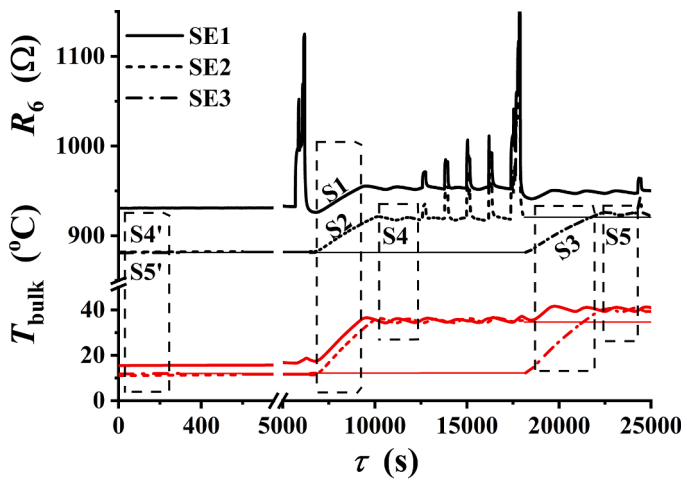

Fig. 10. Different methods for determining the resistance-temperature coefficients of local temperature sensors in space experiments.

and then no change in the electrical performance of each sensor after the corresponding preheating phase. Fig. 11 shows the five data points obtained from the processes mentioned above. The deviation is within ±0.6%. The above modified syn-calibration procedure is verified by using ground experiment data. The uncertainty of local temperature measurement is estimated to be within the range of ±1.0 °C both on the ground and in space.

Additionally, the relatively thick film thickness of the main heater, as well as its isolation from the working fluid, is found to result in its performance being different from those of the local temperature sensors. The overheating in the normal pool boiling phase in each stage has no obvious influence on the electrical performance of the main heater. Thus, the following syn-calibration procedure is used for calibrating the relation between the back-side temperature and the measured signals of the heating voltage U_H across AIN16 and AIN17 shown in Fig. 5 and the reference voltage U_R across AIN17 and AIN18. Considering that the temperature distribution in the vicinity of the integrated microheater may be relatively uniform before the main heater is electrified, the bulk liquid temperature will be equal to the back-side temperature of the substrate of the integrated microheater and correlated to the outputs U_H and U_R immediately after the main heater is electrified. Fig. 12 shows the difference between the bulk liquid temperature and the calculated heating temperature immediately after the main heater is electrified. The uncertainty will evidently also be within the range of ±1.0 °C both on the ground and in space.

3.3. Data reduction for nominal and transient heat flux

Heat conduction inside the substrate is a transient process, especially at the beginning of heating and after boiling inception. The process, however, will tend to a steady state, or at least a quasi-steady state in the statistical sense, after a sufficiently long time in the experiments using the steady heating method. A one-dimensional, steady-state heat conduction equation, namely,

$$q_s = \lambda \Delta T / \Delta x = \lambda \left(T_{back} - T_{top}\right) / \Delta x \tag{1}$$

is used to calculate the nominal steady heat flux across the substrate of the integrated microheater. Moreover, a genetic algorithm-based model is constructed for the one-dimensional transient inverse heat conduction problem inside the heating solid wall during the boiling process [39]. Based on this algorithm, the transient heat flux on the top side and back side of the substrate during boiling processes can be calculated with high accuracy and robustness, which is verified by a benchmark based on the transient half-plane heat conduction problem with an accurate solution.

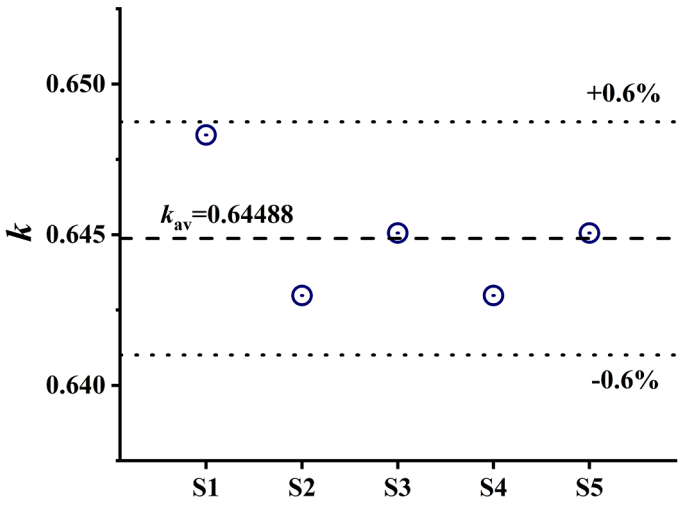

Fig. 11. Resistance-temperature coefficient of local temperature sensor T6.

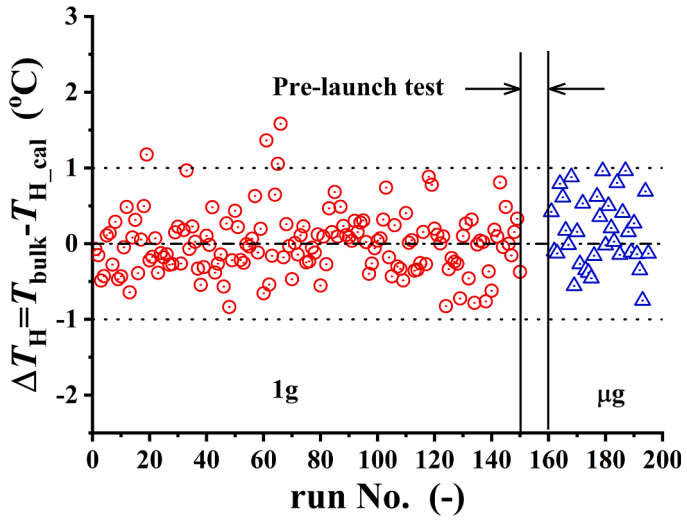

Fig. 12. Deviation of the calibrated back-side temperature both on the ground and in space.

Typical temperature and heat flux data in SE1/1.5 are shown in Fig. 13. Here, the top-side temperature is calculated by averaging the outputs of the ten local temperature sensors on the heater surface, while the back-side temperature is calculated based on the outputs relevant to the main heater. The thermal diffusivity/conductivity λ of the substrate of the integrated microheater takes the corresponding value at the average temperature of the back- and top-side temperatures.

3.4. Non-condensable gas concentration

A degassing procedure with repeated vacuum application and heating is used to reduce the air concentration in the bulk liquid. A separate test indicates that the residual air concentration will be lower than 200 (μmoles of air)/(mole of FC-72). The real air concentration in the bulk liquid filled in the liquid chamber is estimated using Henry's law,

$$c_g = H p_g \tag{2}$$

based on the measured bulk liquid temperature and pressure inside the liquid chamber during the ground thermal test of the SOBER-SJ10 device before the launch and during the first calm phase of stage 5 in SE1 (Fig. 14). The gas partial pressure p_g above the liquid is determined by

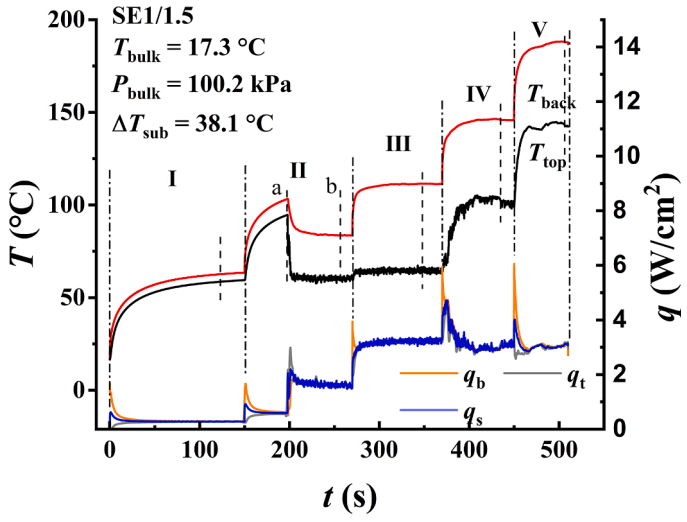

Fig. 13. Temperature and heat flux on the top and back sides in SE1/1.5.

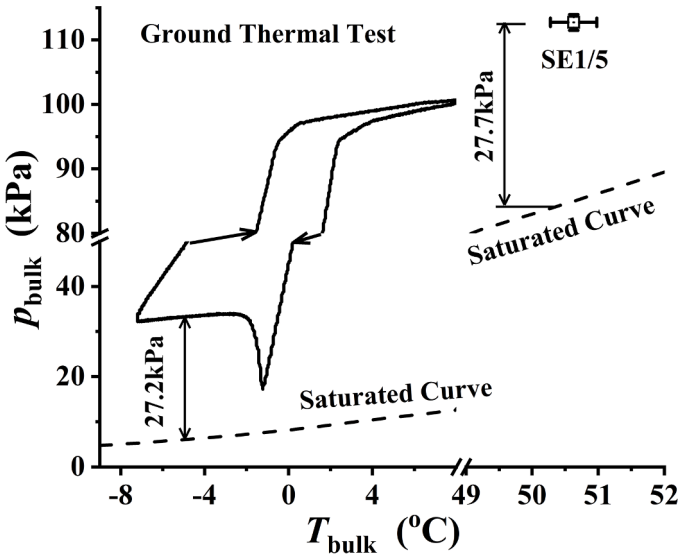

Fig. 14. Non-condensable gas concentration in ground thermal test and space experiments.

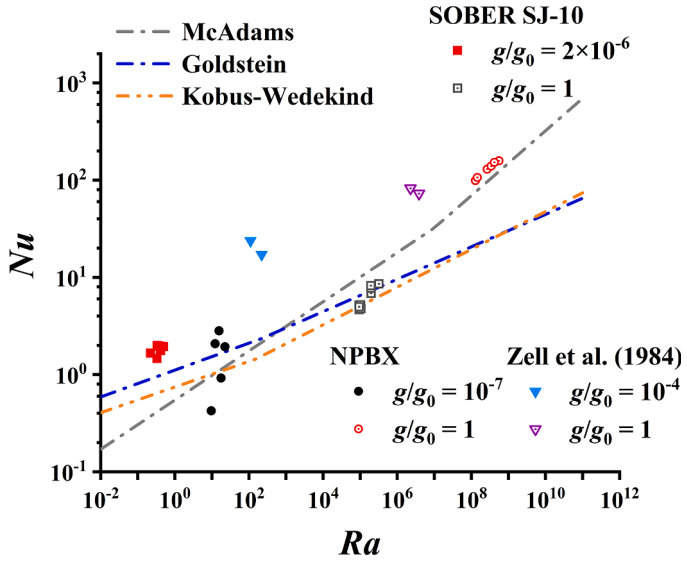

Fig. 15. Single-phase heat transfer in normal and microgravity conditions.

$$p_g = p_{total} - p_{sat}(T_{bulk}) \tag{3}$$

where p_{sat} is the saturation pressure of the liquid at the measured bulk liquid temperature T_{bulk}, while p_{total} is the total pressure above the gas–liquid surface.

During the ground thermal test of the SOBER-SJ10 device before the launch, there is a sharp decline in the pressure inside the liquid chamber with decreasing bulk liquid temperature to near 0 °C. There is then an abrupt jump to a nearly constant value, with a very slight decrease with further decreasing temperature below −1 °C. This indicates that a vapor/air phase exists above the liquid inside the liquid chamber, which is caused by the fixed volume after the bellows stop is activated. Considering the static pressure difference of 3.0 kPa caused by the height of the gas–liquid surface compared to the pressure sensors in normal gravity, the air partial pressure above the liquid can be estimated as 24.2 kPa.

During the first calm phase of stage 5 in SE1, the CCD images show that a large vapor bubble generated in the previous normal pool boiling phase did not completely condense into liquid because of low subcooling and insufficient condensation time. Excluding the effects of bulk liquid temperature adjustment and the small curvature of the existing vapor bubble, the air partial pressure above the liquid can be estimated as 27.7 kPa.

Henry's constant H in Eq. (2) is shown to be a function of temperature only. However, detailed data on constant H variation with temperature are unavailable. Considering the results from different studies [40–42], a value of 5.5×10^{-8} mol/(mole·Pa) for the Henry's constant of air in FC-72 is used in the present study. No data are available for nitrogen dissolved in FC-72. The air concentration can thus be estimated as $1.3\sim1.5 \times 10^3$ (μmoles of air)/(mole of FC-72) based on the test data.

4. Results and discussion

4.1. Single-Phase heat transfer

Fig. 15 shows the measured results of single-phase heat transfer without boiling in both space and ground experiments. Several commonly used empirical correlations for single-phase natural convection (Table 2), as well as the data of other research projects [18,43-47], are also shown for comparison. The applicable range of parameters of different correlations is extrapolated to cover the low Ra in microgravity. Here, based on the equivalent diameter $L_h = \frac{A}{P}$, where A and P denote the effective heating area and the corresponding perimeter of the heater surface, respectively, the Nusselt number (Nu) and the Rayleigh number (Ra) are defined as follows:

Table 2
. Parameters of natural convection correlations.

Author(s)	Correlation for natural convection
McAdmas	$Nu = 0.54Ra^{1/4}$, $10^4<Ra<10^7$
	$Nu = 0.15Ra^{1/3}$, $10^7<Ra<10^{11}$
Goldstein	$Nu = 0.59Ra^{1/4}$, $1<Ra<200$
	$Nu = 0.96Ra^{1/6}$, $200<Ra<10^4$
Kobus-Wedekind	$Nu = 0.738Ra^{0.13}$, $5<Ra<156$
	$Nu = 0.546Ra^{0.194}$, $156<Ra<5\times10^5$

$$Nu = hL_h/\lambda = qL_h/\lambda(T_{top} - T_{bulk}) \tag{4}$$

$$Ra = g\beta(T_{top} - T_{bulk})L_h^3/\nu\alpha \tag{5}$$

in which h, q and g denote the heat transfer coefficient, heat flux and gravity, respectively, while λ, β, ν and α denote the thermal conductivity, expansion coefficient, kinematic viscosity and thermal diffusivity of the fluid, respectively.

According to Zhao et al. [48] and Wang et al. [49], the total quasi-stable-state acceleration aboard satellite SJ-10 during its in-orbit flight is approximately 2×10^{-6} g_0, caused by atmospheric friction and the tidal force. The quasi-stable-state acceleration is approximately 10^{-6} g_0 to 10^{-5} g_0 when the attitude thrusters work and not more than 3×10^{-5} g_0, caused by the attitude angle rate. A value of 2×10^{-6} g_0 is used for the residual gravity in calculating Ra because no attitude thrusters worked according to the requirements of the space experiments of SOBER-SJ10. All natural convection experiments on SJ-10 were conducted at approximately atmospheric pressure with subcooled liquid. Note that data were obtained at earth gravity (Ra=10^4–10^6) and microgravity (Ra=10^{-2}–10^{-1}) before nucleate boiling occurred. For a period of time after each heating state change in Fig. 15, the input heat flux q_b and output heat flux q_t tend to be consistent, and quasi-stable natural convection is established. Replaying the recorded CCD video, there clearly exist discrete shadow stripes swaying away from the heater surface after the main heater is switched on and before the incipience of boiling. This provides some evidence of the existence of single-phase natural convection in the present space experiments.

A fairly good agreement between the present ground experiment data and the natural convection correlations of Kobus-Wedekind and Goldstein is maintained, which shows that the experimental measurement and the heat flux calculation method are reliable. However, the *Nu* value predicted by the natural convection correlation is smaller than the experimental results in microgravity. This is due to the existence of gravity fluctuations in the space experiment, which drives the flow of liquid near the heating surface and induces convection.

Kostoglou et al. [50,51] analyzed experimental data of heat transfer from submillimeter spheroidal heaters in different gravities of parabolic flights and found that no natural convection heat transfer appears for *Ra* smaller than a threshold value of approximately 0.55 based on the present characteristic length definition. The *Ra* in the present space experiments is in the range of 0.3 to 1 at 2×10^{-6} g_0. Considering the upper limit of the residual gravity, however, the actual value of *Ra* may be right-shifted by approximately one order of magnitude and then may be slightly greater than the above threshold value of 0.55. Regardless of the presence or absence of fluctuations in gravity, single-phase heat transfer of the flat plate still exists in low *Ra* conditions. The experimental data in microgravity are still in good agreement with the predictions of the Goldstein correlation for single-phase natural convection.

4.2. Pool boiling phenomena in microgravity

Fig. 13 shows a typical history of the average temperature on the top and back sides of the substrate of the integrated microheater and the nominal heat flux across the substrate or transfer from the heater surface to the working fluid in SE1/1.5, a typical normal pool boiling phase with the highest subcooling of 40.1 °C in the present space experiments. The transient bottom surface input heat flux q_b, top heating surface heat flux q_t and pseudo-steady-state heat flux q_s calculated based on the steady-state formula are shown simultaneously. The pressure inside the liquid chamber is 100.2 kPa and remains constant throughout the boiling phase. The corresponding bubble behavior is shown in Fig. 16.

When the experiment starts and the main heater switches on, the initial heating voltage is 2 V. As shown in Fig. 13, the input heat flux of the bottom surface q_b initially rapidly decreases, while the heat flux of the heating surface q_t rapidly increases. The two heat fluxes gradually become the same, which indicates that the heat conduction inside the substrate becomes steady. No bubbles are observed, so it is a single-phase heat transfer process. After 150 s, the heating voltage of the main heater switches to 3 V, and the temperatures of the top and bottom surface rise thereupon. At 228 s, the average temperature of the top surface reaches 94.7 °C, and then, boiling begins to occur on the surface.

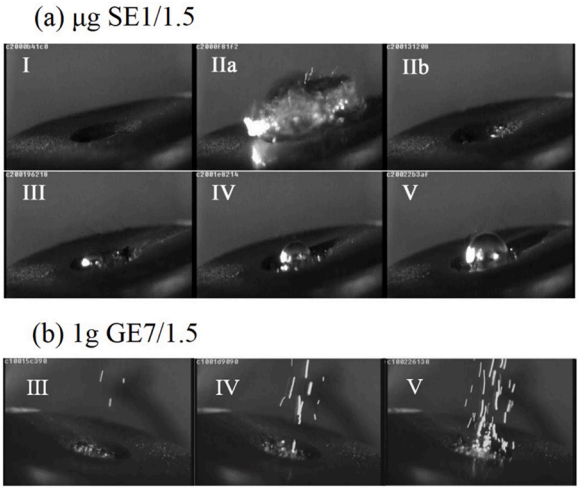

Fig. 16. Bubble behavior in space and ground experiment. (a) SE1/1.5; (b) GE7/1.5 The labels correspond to different heating power steps.

From the CCD image in Fig. 16(a) IIa, the first bubble is explosively generated due to the extremely high superheating on the surface. The bubble mass absorbs massive heat from the liquid and the surface adjacent to it, which causes a drastic temperature drop on the top surface, followed by a temperature decrease on the bottom surface. The subsequently generated vapor pushes the first generated bubble away from the surface, and the remaining part forms a smaller bubble cluster. This bubble cluster is maintained on top of the heater surface and continuously absorbs small bubbles generated adjacent to it. However, because the bulk liquid is subcooled, the volume of the bubble cluster decreases because of condensation on the bubble cap, as shown in Fig. 16(a) IIb. After the onset of boiling, the heat flux of the heating surface will jump high and then rapidly decay. The calculated three different heat fluxes q_b, q_t and q_s gradually converge. Meanwhile, the temperature of the bottom surface quickly decreases in the first 5 s after the onset of boiling (at approximately 200 s), and then, the bottom temperature becomes relatively constant. The steady states of the temperature and heat flux indicate that the heat transfer inside the heater becomes steady, and the experiment enters a steady nucleate pool boiling stage.

At 270 s, the heating voltage switches to 4 V. The temperature of the bottom surface rapidly increases in the first 10 s and reaches a relatively constant value of 111.5 °C, which is 27.0 °C higher than that in the previous stage IIb. Boiling bubbles continue to be generated, move and merge on the top surface, and the bubbles are larger and generated more frequently than in stage IIb, as shown in Fig. 16(a) III. The temperature on the top surface only increases by 5.0 °C. No large bubble mass is formed, so this boiling still belongs to the nucleate boiling process.

At 370 s, the heating voltage switches to 5 V, and the temperatures of the top and bottom surfaces start to increase again. As shown in Fig. 16 (a) IV, the bubble mass absorbs small bubbles that are generated underneath it as a vapor sink and continuously grows on top of the surface. The top surface gradually becomes partially covered with vapor, which reduces heat transfer from the heater to the bulk liquid. At the end of this stage, the temperatures of the top and bottom surfaces are both approximately 25.0 °C higher than those in the previous stage, while the heat flux is slightly reduced. This indicates a deterioration in heat transfer, and boiling becomes transition boiling.

At 420 s, the heating voltage switches to 6 V. The large bubble mass continues to grow and finally completely covers the top surface, as shown in Fig. 16(a) V. Before heating stops at 510 s, the temperatures of the top and bottom surfaces reach 188 °C and 155 °C, respectively, while the heat flux slightly decreases. The boiling gradually becomes film boiling, and most of the heating surface area is covered by steam, resulting in a further decrease in the heat transfer efficiency. After heating stops, the temperatures of the top and bottom surfaces decrease, and the bubble diminishes in size and completely condenses back to liquid.

The bubble dynamics characteristics of the ground boiling are simultaneously shown in the Fig. 16(b) for comparison. Relevant pictures are taken from GE7/1.5 (stage III-V). Experiment status in GE7/1.5 is consistent with the space experiment. In normal gravity, the state of nucleate boiling is maintained after the initiation of boiling, and the bubbles generated by nucleation quickly leave the heating surface under the action of buoyancy to form a strip-shaped trajectory.

Fig. 17 shows that under the same heating voltage, ground experiments are always maintained in the nucleate boiling state. In space experiments, boiling starts to transition into the film boiling region at a CHF of 4.51 W/cm^2, which indicates that the end of the nucleate boiling stage under microgravity significantly corresponds to a lower heat flux than that on the ground. This results from the difference in bubble shape and the remaining vapor merging characteristic. Due to the lack of buoyancy, the bubbles are always attached to the heating surface and gradually grow, preventing contact between the heating surface and the liquid. The existence of vapor will lead to deterioration of heat transfer in a partial area of the heating surface, and the large vapor mass will

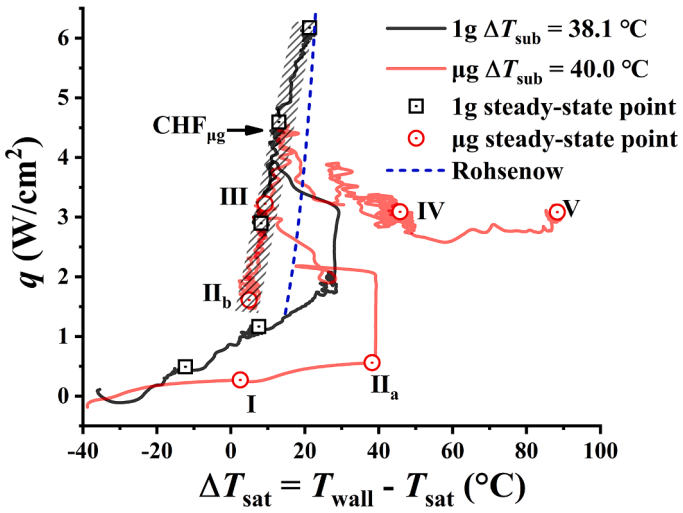

Fig. 17. Comparison of boiling curves in GE7/1.5 and SE1/1.5.

eventually make the boiling reach the CHF at a lower wall superheat, making the boiling become transition boiling earlier than in the ground experiment under a similar heating voltage. Subsequently, the temperature of the heating surface rapidly rises, and the boiling develops into transition boiling or even film boiling depending on whether the bubble completely covers the heating surface.

4.3. Comparison of pool boiling experiment results under different subcooling conditions

The nucleate pool boiling results under different subcooling conditions are plotted in Fig. 18. The black and red lines are the normal pool boiling results calculated by the genetic algorithm in normal and microgravity, respectively. Due to the anomaly of the integrated heater that occurred during the supplementary experiments, only the comparative experimental data from the extended space experiment of SE2/2.5 are valid, which are plotted in Fig. 18a by the blue line. The dots on lines represent the steady state of five different heating stages of normal pool boiling experiments. Moreover, Roman numerals are used in Fig. 18 to highlight the heating stage when boiling occurs. For example, Ia indicates a single-phase heat transfer steady state before the onset of boiling, while Ib indicates that the system reaches a steady state

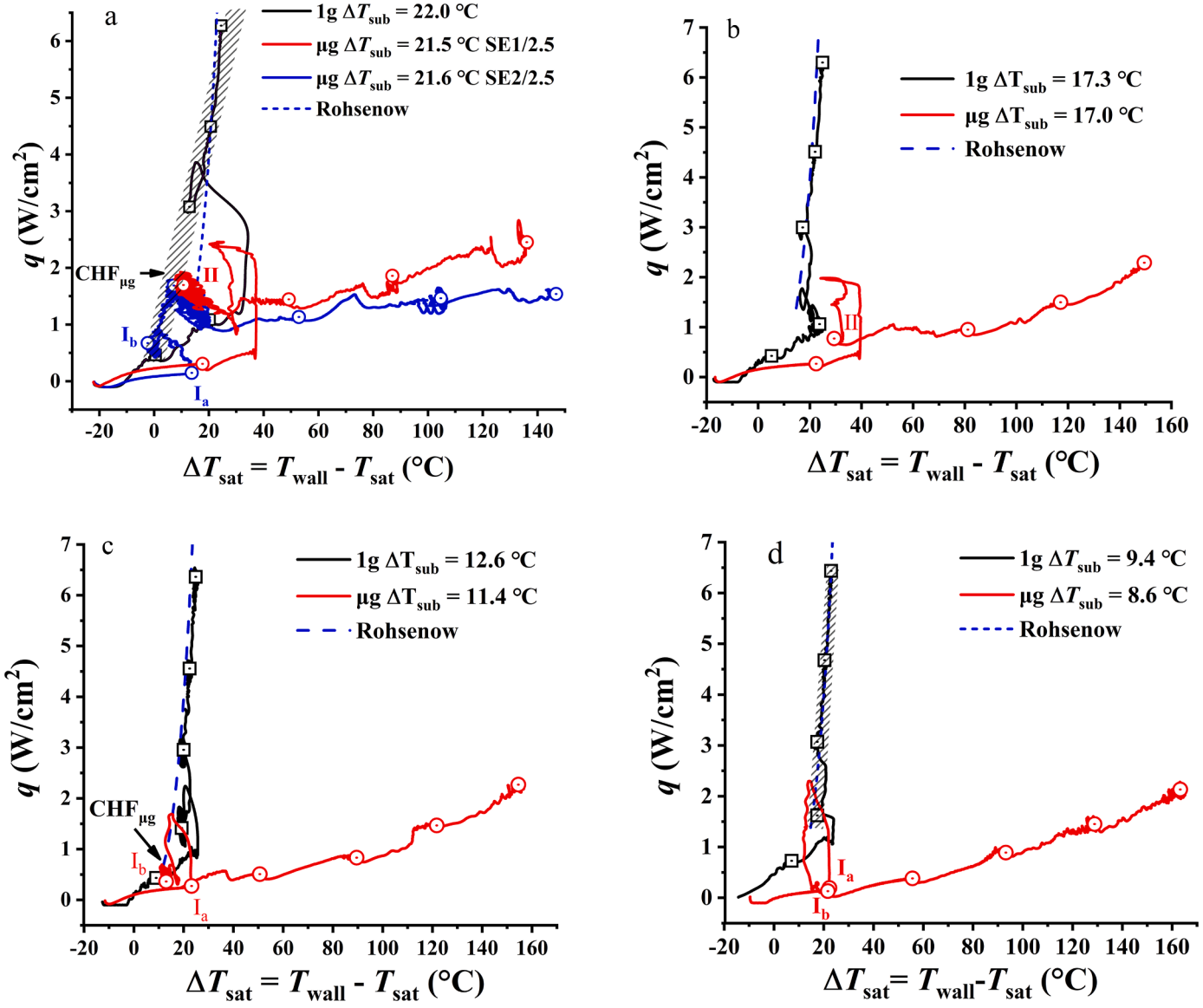

Fig. 18. Boiling curves under different subcooling conditions.

after the onset of boiling. In some cases, when the heating stage is changed, boiling quickly occurs, and the single-phase heat transfer does not reach a steady state. Only a single number is used to indicate the steady-state stage after boiling in this heating stage. Boiling more easily occurs in the early heating stage as the temperature of the liquid increases.

Nucleate pool boiling can be maintained under both normal and microgravity under high subcooling conditions, and the heat flux obtained in microgravity experiments is lower than that in normal gravity. The burst of boiling is accompanied by a peak of the heat flux. The overheating of the heating surface and its nearby liquid layer leads to rapid vaporization, and a large amount of heat is absorbed from the superheated liquid layer and the surface of the heating substrate, resulting in a decrease in the wall temperature. After the burst of boiling, the heat flux first decreases and then gradually increases as the temperature of the heating surface increases. Its trajectory is the heat flux curve.

After the onset of boiling, the generated gas merges on the heating surface to form bubbles. When the liquid subcooling is high, the volume of the bubble is small. The subcooled bulk far from the heating surface will cause part of the vapor to condense and disappear, and the continuous condensation at the top of the bubbles will maintain nucleate boiling (Fig. 17, Fig. 18a). When the liquid subcooling is low, the generated gas forms larger bubbles, covering most of the heating surface. When the bubble size exceeds the heating surface, the temperature of the heating surface sharply rises, nucleate boiling cannot be maintained for a long time, and transition boiling more easily occurs (Fig. 18b, c, d).

Affected by the high bulk subcooling, the boiling under the condition of a low heat flux is not fully developed. As shown in Fig. 17, there is a certain deviation compared with the value predicted from the Rohsenow correlation, but the deviation gradually vanishes with increasing wall temperature. Additionally, such deviations diminish as the liquid subcooling decreases. Under the same liquid subcooling, the initial heat flux of the nucleate boiling curve under microgravity is much lower than that on the ground. In addition, a relatively low CHF in microgravity is observed when the boiling deviates from nucleate boiling and transforms into transition boiling or film boiling. The locations of the CHF in microgravity experiments are also plotted in Fig. 18. No nucleate pool boiling data or CHF values are obtained in the b and d subcooling conditions because the single-phase region is directly converted to film boiling, in which the heating surface is quickly covered by bubble clusters and CHF could not be captured.

For the cases shown in Fig. 18, the CHF varies from 0.59 to 4.51 W/cm^2. The predicted CHF values are obtained from the Kutateladze-Zuber correlation suitable for saturated liquids. The Ivey-Morris semiempirical CHF correlation [52] is also used to calculate the CHF in subcooled boiling:

$$q_{K-Z} = 0.131\rho_v^{1/2}h_{fg}[\sigma(\rho_l-\rho_v)g]^{1/4} \tag{7}$$

$$q_{CHF} = q_{K-Z}\left[1+0.102(\rho_l/\rho_v)^{0.75}\frac{\Delta T_{sub}c_p}{h_{fg}}\right] \tag{8}$$

Here, the observed and predicted CHF values are shown in Table 3. The CHF values in microgravity experiments are obviously higher than those predicted from the Ivey-Morris correlation, which indicates that liquid subcooling has a great influence on the CHF in microgravity. The vapor bubble characteristics in microgravity are different from those in normal gravity. The CHF is related to the coverage of bubbles on the heating surface, and the volume of the bubbles is simultaneously affected by the liquid subcooling and heating power. Lower liquid subcooling and higher heating power will result in larger bubble volumes and easier complete coverage of the heating surface, resulting in an easier transition from nucleate boiling to film boiling. Mechanisms underlying ground-based CHF prediction correlations do not apply to microgravity environments. Under microgravity, liquid subcooling, the heating power and the bubble characteristics on the heating surface have an important influence on the boiling state. Any correlations developed for boiling and the CHF under microgravity conditions must account for these factors.

Table 3
. Comparison of CHF in microgravity and normal gravity (unit W/cm^2).

Subcooling (°C)	1 g Pre.	μg Pre.	μg Exp.
38.1	29.95	0.64	4.51
21.5	23.29	0.50	2.01
11.4	18.33	0.39	0.59
0	12.80	0.29	–

4.4. *Nucleate boiling experiment results under different subcooling conditions*

A comparison of nucleate pool boiling results in normal and microgravity with different liquid subcooling conditions is shown in Fig. 19. As shown in Fig. 19, the slope of the boiling curve increases with decreasing subcooling. The steady states of nucleate boiling in microgravity and normal gravity are marked with symbols. Moreover, the CHF is not reached in ground experiments, so only the onset of nucleate boiling in normal gravity is indicated by black dots. In microgravity, bubbles maintain heat and mass transfer through evaporation at the bottom and condensation at the top. Higher liquid supercooling will increase the condensation rate of the gas-liquid interface of the bubbles, inhibit the growth of the bubble volume, and improve the heat transfer efficiency. When superheating is low, the heat transfer efficiency is strongly influenced by subcooling, and increasing subcooling enhances the heat transfer efficiency. However, in terrestrial gravity, the influence of subcooling on the boiling curve decreases, and the boiling curves in ground gravity tend to merge at a high heat flux with increasing superheating. Compared to microgravity conditions, boiling on the ground is less affected by liquid subcooling.

The NPBX results from Warrier et al. [18] and the MABE results from Raj et al. [15] are also plotted in Fig. 19 and compared to the present results. The NPBX utilized a polished aluminum disk 89.5 mm in diameter with 5 artificial cavities on the top surface as the test surface. Microheater arrays consisting of 96 individually controlled platinum resistance heaters were used in the MABE. A heating area 7.0 mm in diameter was used in the reported experiments, which is close to the diameter of the heater in the present work. Both of these experiments were conducted in the BXF utilizing the ISS as a microgravity research

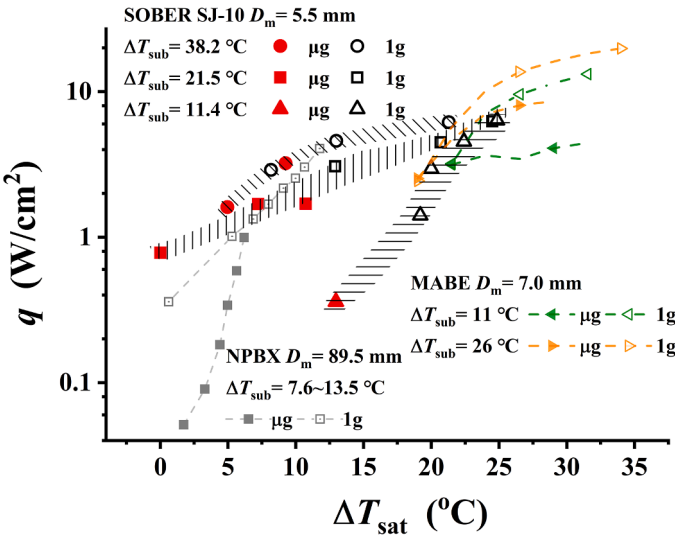

Fig. 19. Comparison of nucleate boiling results.

platform and perfluoro-n-hexane as the working fluid. The experimental conditions for the results shown in Fig. 19 are presented in Table 4. As shown in Fig. 19, an increase in subcooling enhances heat transfer in the NPBX results and in the present results in both normal and microgravity. The heat flux obtained in microgravity is lower than that in normal gravity in all three studies. However, under close subcooling conditions, the present results are close to the MABE results, in which the superheating is much higher than that in the NPBX under the same heat flux. The heat transfer efficiency decreases with decreasing heater diameter. When subcooling is increased in the present work, boiling has a higher heat transfer efficiency, and the CHF point at the end of the nucleate boiling curve corresponds to a higher heat flux. Higher liquid subcooling suppresses the coverage of the heater surface by the stable spherical bubble vapor mass, thereby increasing the wall superheating when nucleate boiling reaches the CHF.

Note that due to the complexity of boiling, the position and data of the boiling curves in these boiling studies are quite different when only the heater is different and other experimental conditions are similar in microgravity. This suggests that the boiling data of different heaters cannot be directly compared with each other, which results in a lack of sufficient directly comparable data to study the effect of gravity on boiling. In view of this, the Gravity Scaling Law of Pool Boiling Heat Transfer and Bubble Thermal Dynamic Behaviors project is proposed [53]. The long-term stable variable gravity environment provided by the Varying Gravity Rack of the China Space Station is planned to be used to carry out the variable gravity boiling experiments, aiming to reveal the effect of gravity on the boiling heat transfer.

5. Conclusions

- Pool boiling experiments were successfully conducted onboard the SJ-10 satellite. An improved method was developed based on the data to solve the calibration problem. The uncertainties of the local temperature and main heater temperature are no more than ±1.0 °C during the space experiments.
- Single-phase convective heat transfer was observed in microgravity. The present results indicate that single-phase convection could still be maintained under lower Rayleigh number conditions, and the extended classical correlations of natural convective heat transfer could still predict the results in the present study.
- The bubble behavior and heat transfer features during the onset of pool boiling in microgravity are different from the results in ground experiments, which indicates that the characteristics of bubbles on the heater surface will have a strong effect on the heat transfer process in microgravity.
- The comparison of pool boiling curves in normal and microgravity conditions indicates that nucleate boiling curves under the same subcooling partially overlap. The initial boiling under microgravity conditions corresponds to a lower heat flux than that on the ground.
- As the degree of subcooling increases, under microgravity conditions, the heat transfer efficiency of nucleate boiling and the CHF increase. However, boiling is less affected by liquid subcooling in normal gravity.

CRediT authorship contribution statement

Peng Liu: Methodology, Conceptualization, Software. **Ke Wu:** Writing – original draft, Investigation, Validation. **Wang-Fang Du:** Data curation, Conceptualization. **Hui-Xiong Li:** Supervision, Resources. **Jian-Fu Zhao:** Supervision, Resources.

Declaration of Competing Interest

The authors declare that they have no known competing financial interests or personal relationships that could have appeared to influence the work reported in this paper.

Table 4
Comparison of experimental conditions.

	Heater diameter (mm)	Subcooling (°C)	Pressure (kPa)	dissolved gas content (ppm)
SOBER	5.5	10–40	100.2–113.6	1300–1500
NPBX	89.5	7.6–13.5	125	261
MABE	4.2–7.0	11–26	101.0	<250

Data availability

Data will be made available on request.

Acknowledgment

The authors thank Dr. Zhao from Dalian University of Technology for his effective guidance and help in data analysis. This research is supported financially by the National Key R&D Program of China under the grant of 2022YFF0503502, Joint Fund between the Chinese Academy of Sciences (CAS) and National Natural Science Foundation of China (NSFC) under the grant of U1738105 and the Strategic Priority Research Program on Space Science, the Chinese Academy of Sciences under the grants of XDA04020404 and XDA04020202–04.

References

[1] J. Straub, Boiling heat transfer and bubble dynamics in microgravity, Adv. Heat Transf. 35 (2001) 57–172.
[2] P. Di Marco, W. Grassi, Effect of force fields on pool boiling flow patterns in normal and reduced gravity, Heat Mass Transf. 45 (7) (2009) 959–966.
[3] J. Kim, Review of nucleate pool boiling bubble heat transfer mechanisms, Int. J. Multiph. Flow 35 (12) (2009) 1067–1076.
[4] H. Ohta, S. Baba, Boiling experiments under microgravity conditions, Exp. Heat Transf. 26 (1–5) (2013) 266–295.
[5] C. Colin, O. Kannengieser, W. Bergez, M. Lebon, J. Sebilleau, M. Sagan, S. Tanguy, Pool boiling in microgravity: recent progress and future prospects, C. R. Méc. 345 (1) (2017) 21–34.
[6] J.F. Zhao, Two-phase flow and pool boiling heat transfer in microgravity, Int. J. Multiph. Flow 36 (2010) 135–143.
[7] S.H. Hong, J.X. Wang, Z.J. Gao, C.B. Dang, Review on state-of-the-art research in pool and flow boiling under microgravity, Exp. Therm. Fluid Sci. 144 (2023), 110848.
[8] J. Kim, J. Benton, D. Wisniewski, Pool boiling heat transfer on small heaters: effect of gravity and subcooling, Int. J. Heat Mass Transf. 45 (2002) 3919–3932.
[9] C.D. Henry, J. Kim, A study of the effects of heater size, subcooling, and gravity level on pool boiling heat transfer, Int. J. Heat Fluid Flow 25 (2004) 262–273.
[10] C.D. Henry, J. Kim, J. McQuillen, Dissolved gas effects on thermocapillary convection during subcooled boiling in reduced gravity environments, Int. J. Heat Mass Transf. 42 (2006) 919–928.
[11] R. Raj, J. Kim, Heater size and gravity based pool boiling regime map: transition criteria between buoyancy and surface tension dominated boiling, J. Heat Mass Transf. 132 (9) (2010), 091503.
[12] R. Raj, J. Kim, J. Mcquillen, Subcooled pool boiling in variable gravity environments, J. Heat Transf. 131 (9) (2009), 091502.
[13] R. Raj, J. Kim, J. Mcquillen, Gravity scaling parameter for pool boiling heat transfer, J. Heat Mass Transf. 132 (9) (2010), 091502.
[14] R. Raj, J. Kim, J. Mcquillen, On the scaling of pool boiling heat flux with gravity and heater size, J. Heat Mass Transf. 134 (2012), 011502.
[15] R. Raj, J. Kim, J. McQuillen, Pool boiling heat transfer on the international space station: experimental results and model verification, J. Heat Mass Transf. 134 (2012), 101504. -1.
[16] O. Kawanami, H. Ohta, O. Kabov, Y. Sakata, Y. Kotani, Y. Asada, T. Nagayasu, Y. Shimoto, S. Chikov, P. Queeckers, J. Struab, Heat transfer and bubble behaviors in microgravity pool boiling in ESA parabolic flight experiment, Microgravity Sci. Technol. 21 (Suppl 1) (2009) S3–S8.
[17] V.K. Dhir, G.R. Warrier, E. Aktinol, D. Chao, J. Eggers, W. Sheredy, W. Booth, Nucleate pool boiling experiments (NPBX) on the international space station, Microgravity Sci. Technol. 24 (2012) 307–325.
[18] G.R. Warrier, V.K. Dhir, D.F. Chao, Nucleate pool boiling experiment (NPBX) in microgravity: international space station, Int. J. Heat Mass Transf. 83 (2015) 781–798.
[19] J.F. Zhao, J. Li, N. Yan, S.F. Wang, Bubble behavior and heat transfer in quasi-steady pool boiling in microgravity, Microgravity Sci. Technol. 21 (2009) S175–S183.

[20] Y.F. Xue, J.F. Zhao, J.J. Wei, J. Li, D. Guo, W. S.X, Experimental study of nucleate pool boiling of FC-72 on smooth surface under microgravity, Microgravity Sci. Tech. 23 (2011) S75–S85.
[21] Y. Zhang, J. Zhou, W. Zhou, B.J. Qi, J.J. Wei, CHF correlation of boiling in FC-72 with micro-pin-fins for electronics cooling, Appl. Therm. Eng. 138 (2018) 494–500.
[22] P. Di Marco, W. Grassi, Effect of force fields on pool boiling flow patterns in normal and reduced gravity, Heat Mass Transf. 45 (7) (2009) 959–966.
[23] P. Di Marco, W. Grassi, Effects of external electric field on pool boiling: comparison of terrestrial and microgravity data in the ARIEL experiment, Exp. Therm. Fluid Sci. 35 (5) (2011) 780–787.
[24] N. Schweizer, P. Di Marco, P. Stephan, Investigation of wall temperature and heat flux distribution during nucleate boiling in the presence of an electric field and in variable gravity, Exp. Therm. Fluid Sci. 44 (2013) 419–430.
[25] S. Fischer, S. Herbert, A. Sielaff, E.M. Slomski, P. Stephan, M. Oechsner, Experimental investigation of nucleate boiling on a thermal capacitive heater under variable gravity conditions, Microgravity Sci. Tech. 24 (2012) 139–146.
[26] S. Narayan, T. Singh, S. Singh, A. Srivastava, Experiments on the effects of varying subcooled conditions on the dynamics of single vapor bubble and heat transfer rates in nucleate pool boiling regime, Int. J. Heat and Mass Transf. 134 (2019) 85–100.
[27] S. Narayan, T. Singh, A. Srivastava, Experiments on pool boiling regimes and bubble departure characteristics of single vapor bubble under subcooled bulk conditions, Exp. Therm. Fluid Sci. 111 (2020), 109943.
[28] G.K. Sinha, S. Narayan, A. Srivastava, Microlayer dynamics during the growth process of a single vapour bubble under subcooled flow boiling conditions, J. Fluid Mech. 931 (2022) A23.
[29] A. Sielaff, D. Mangini, O. Kabov, et al., The multiscale boiling investigation on-board the International Space Station: an overview, Appl. Therm. Eng. 205 (2022), 117932.
[30] I. Nejati, A. Sielaff, B. Franz, et al., Experimental investigation of single bubble nucleate boiling in microgravity, Microgravity Sci. Technol. 32 (2020) 597–607.
[31] O. Oikonomidou, S. Evgenidis, C. Argyropoulos, Bubble growth analysis during subcooled boiling experiments on-board the international space station: benchmark image analysis, Adv. Colloid Interface Sci. 38 (2022), 102751.
[32] A.I. Garivalis, P. Di Marco, Isolated bubbles growing and detaching within an electric field in microgravity, Appl. Therm. Eng. 212 (2022), 118538.
[33] K. Wu, Z.D. Li, J.F. Zhao, H.X. Li, K. Li, Partial nucleate pool boiling at low heat flux: preliminary ground test for SOBER-SJ10, Microgravity Sci. Tech. 28 (2016) 165–178.
[34] W.F. Du, J.F. Zhao, Gravity scaling law of heat transfer in nucleate pool boiling, Chin. Sci. Bull. 65 (2020) 1629–1637.
[35] W.R. Hu, J.F. Zhao, M. Long, X.W. Zhang, Q.S. Liu, M.Y. Hou, Q. Kang, Y.R. Wang, S.H. Xu, W.J. Kong, Space program SJ-10 of microgravity research, Microgravity Sci. Tech. 26 (2014) 159–169.
[36] W.R. Hu, B.C. Tang, Q. Kang, Progress of microgravity experimental satellite SJ-10, Aeron. Aero. Open Access J. 1 (3) (2017) 00016.
[37] L. Zhang, Z.D. Li, K. Li, H.X. Li, J.F. Zhao, Influence of heater thermal capacity on bubble dynamics and heat transfer in nucleate pool boiling, Appl. Therm. Eng. 88 (2015) 118–126.
[38] Z.D. Li, L. Zhang, J.F. Zhao, K. Li, K. Wu, Numerical simulation of bubble dynamics and heat transfer with transient thermal response of solid wall during pool boiling of FC-72, Int. J. Heat Mass Transf. 84 (2015) 409–418.
[39] P. Liu, W.F. Du, K. Wu, J.F. Zhao, H.X. Li, Study on performance of pool boiling heat transfer in SOBER-SJ10 based on genetic algorithem, J. Eng. Thermophys. 42 (2021) 1784–1790.
[40] Product Manual, Fluorinert Electronic liquids, Commercial Chemical Products Div, Co., St. Paul, 1987, 3MMN, USA.
[41] S.M. You, Pool boiling heat transfer with highly-wetting dielectric fluids. Ph.D. Thesis, University of Minnesota, Minneapolis, MN, 1990. https://www.proquest.com/docview/303834406?pq-origsite=wos&accountid=178531.
[42] V. Vins, V. Vacek, Effect of gas impurities on the throttling process of fluorocarbon refrigerants: estimation of the Henry's law constant, J. Chem. Eng. Data 54 (2009) 2395–2403.
[43] J.L. Parker, M.S. El-Genk, Enhanced saturation and subcooled boiling of FC-72 dielectric liquid, Int. J. Heat Mass Transf. 48 (2005) 3738–3752.
[44] W.H. McAdams, Heat Transmission, 3rd ed., McGraw-Hill, New York, 1954.
[45] R.J. Goldstein, E.M. Sparrow, D.C. Jones, Natural-convection mass-transfer adjacent to horizontal plates, Int. J. Heat Mass Transf. 16 (5) (1973) 1025–1035.
[46] C.J. Kobus, G.L. Wedekind, An experimental investigation into forced, natural and combined forced and natural convective heat-transfer from stationary isothermal circular disk, Int. J. Heat Mass Transf. 38 (18) (1995) 3329–3339.
[47] C.J. Kobus, G.L. Wedekind, An experimental investigation into natural convection heat transfer from horizontal isothermal circular disks, Int. J. Heat Mass Transf. 44 (17) (2001) 3381–3384.
[48] H.G. Zhao, J.W. Qiu, B.C. Tang, Q. Kang, W.R. Hu, The SJ-10 recoverable microgravity satellite of China, J. Space Explor. 4 (3) (2016) 1–9.
[49] Y. Wang, H.G. Zhao, Y.C. Zhang, J.W. Qiu, X.Y. Mao, X.S. Wang, Establishing and evaluation of the microgravity level in the SJ-10 recoverable satellite, Aerosp. China 17 (4) (2016) 3–13.
[50] M. Kostoglou, S.P. Evgenidis, T.D. Karapantsios, Unexpected natural convection heat transfer for small Rayleigh numbers in external geometry, Int. J. Heat Mass Transf. 64 (2013) 773–782.
[51] M. Kostoglou, S.P. Evgenidis, K.A. Zacharias, T.D. Karapantsios, Heat transfer from small objects in microgravity: experiments and analysis, Int. J. Heat Mass Transf. 54 (2011) 3323–3333.
[52] H.J. Ivey, D.J. Morris, On the Relevance of the Vapor Liquid Exchange Mechanism For Subcooled Boiling At High Pressure, United Kingdom Atomic Energy Authority, Reactor Group, Atomic Energy Establishment, England, 1962.
[53] W.F. Du, P. Liu, J.F. Zhao, X. Li, Z.H. Qiao, F. Ye, H. Guo, W.J. Jiang, Z.G. Li, Boiling water aboard the China Space Station to reveal the gravity influence in boiling phenomenon, Mech. Eng. 44 (2022) 1462–1469.